RSC Advances

PAPER

View Article Online
View Journal | View Issue

Cite this: *RSC Adv.*, 2024, **14**, 26066

Addition of silver nanoparticles to the zinc ferrite/polyaniline composition for boosting its visible photocatalytic degradation

Safanah Sahib Jaafar,[a] Rana Ismael Faeq,[a] Amel Muhson Naji,[b] Olfat A. Nief[a] and Mustafa K. A. Mohammed *[c]

Received 14th July 2024
Accepted 14th August 2024

DOI: 10.1039/d4ra05096g

rsc.li/rsc-advances

Enhancing the photocatalytic activity of $ZnFe_2O_4$ with a good energy band gap to degrade industrial waste under sunlight illumination can help to develop green environments. Here, to improve the photocatalytic efficiency of $ZnFe_2O_4$ ferrites, they were merged with polyaniline (PAni) and silver (Ag) nanoparticles to synthesize Ag@$ZnFe_2O_4$–PAni plasmonic nanostructures. The as-synthesized nanostructures were characterized using a series of advanced characterization techniques to confirm successful formation and investigate photocatalytic improvement origins. It was found that incorporating Ag NPs along with the PAni to $ZnFe_2O_4$ increases its absorption power and red-shifts its energy band gap, which increases the electron–hole production rate by exposure to light in $ZnFe_2O_4$. Contribution of the surface plasmon resonance effect of Ag NPs and conjugated double bonds of PAni to charge transfer mechanisms in Ag@$ZnFe_2O_4$–PAni material increased charge separation during photocatalytic process, boosting the photodegradation performance of $ZnFe_2O_4$.

1 Introduction

With the increase in world population and the industrial development to meet human needs for food, clothing, electrical appliances, *etc.*, the increase in environmental pollution has become a critical challenge.[1,2] This industrial waste affects the water quality of rivers and underground water, and subsequently negatively impact human health and the ecosystem.[3,4] Heavy metal ions, phenols, dyes, polychlorinated biphenyls (PCBs), pharmaceutical drugs, haloacetic acids (HAAs), pesticides, disinfection byproducts (DBPs), and other synthetic chemicals are the main sources of water pollution.[5–8] For years, the Environmental Protection Agency (EPA) and World Health Organization (WHO) have recommended that the world's industries do not discharge contaminated water into their surrounding environments. Various methodologies have been suggested to clean the water before discharging, including, precipitation, ozonation, adsorption, membrane separation, biodegradation, sonodegradation, solvent extraction, and ion exchange.[9–13] These approaches have serious drawbacks, including toxic products, high operating costs, and low elimination rates. In contrast, advanced oxidation photocatalysis offers an ultimate deterioration, cheap, and eco-friendly method to treat wastewater with considerable recyclability.[14,15] The photocatalysis process is used to disinfect the wastewater and eliminate contaminants from water and air. The photocatalyst material promotes the elimination reaction rate of targeted waste from water with the assistance of a light illumination source. During the process, the irradiated light reacts with the photocatalyst material to generate electron–hole pairs. Next, these photo-generated electrons participate in reduction reactions to start the oxidation of holes.[16–18]

In recent years, nano-sized materials were introduced as a primary area of research to find advanced technologies for meeting the world's demands. Nano-sized materials have a considerable surface area, which increases their chemical reaction with other materials. In addition, tunable electrical conductivity and optical properties of nano-sized materials along with their mechanical strength, compared to their bulk counterparts, makes them interesting materials to design different advanced technologies. Nanotechnology suggests cost-effective and efficient materials to use in the remediation of dirty water.[19–23] As mentioned, industrial development and its conflict of interest with the green environment have led to an excessive increase in the pollution of natural water. Developing advanced nanomaterial photocatalysts has emerged as a promising technology to address this concern.[24] Spinel ferrites have attracted environmental research due to their unique features, such as chemical stability, high adsorption capacities, cost-effective preparations, and superparamagnetic capabilities, to employ them as photocatalyst material for water treatment to

[a]*Department of Chemistry, College of Science, Mustansiriyah University, P. O. BOX 14132, Baghdad, Iraq*

[b]*Department of Optics Techniques, Dijlah University College, Al-Masafi Street, Baghdad, 00964, Iraq*

[c]*College of Remote Sensing and Geophysics, Al-Karkh University of Science, Baghdad 10011, Iraq. E-mail: mustafa_kareem97@yahoo.com*

remove pollutants *via* photodegradation mechanism.[25–29] Zinc ferrite ($ZnFe_2O_4$), due to their small band gap, is more favorable for visible photocatalytic degradation of water pollution. However, the net zinc ferrites do not have strong photocatalytic efficiency due to weak charge separation.[30–32]

Yu *et al.*[31] to enhance catalytic activity of zinc ferrites substituted copper metal to $ZnFe_2O_4$ structure. They deduced that the increased catalytic activity of zinc-based ferrite ascribes to the dual active sites of Fe and Cu and oxygen vacancies after Cu substitution. Janani *et al.*[32] decorated $ZnFe_2O_4$ with CdO material to boost the photocatalytic efficiency of $ZnFe_2O_4$. They found that the CdO/$ZnFe_2O_4$ with a high surface area offers more active sites to induce the photocatalysis performance of the system. In addition, they concluded that coupling of $ZnFe_2O_4$ and CdO improved the lifetime of charge carriers and promoted the reaction of photo-generated electrons and holes with dye molecules. Akshhayya *et al.*[33] decorated $ZnFe_2O_4$ with SnS_2 material to accelerate visible light photocatalysis of methylene blue. They observed that the formed interfacial contact in the $ZnFe_2O_4$/SnS_2 system suppresses charge recombination and retains better charge separation. These improvements with high visible-light absorbing ability offer an n-SnS_2/p-$ZnFe_2O_4$ hybrid system with improved photocatalytic activity. Kaushal *et al.*[34] developed a $ZnFe_2O_4$@nitrogen-doped carbon dots hybrid material to decomposite ciprofloxacin and norfloxacin materials under visible light irradiance. They observed that nitrogen-doped carbon dots hybridized with zinc ferrites, which enhanced photocurrent density and surface area. The $ZnFe_2O_4$@nitrogen-doped carbon dots exhibited efficient transfer of charge carriers and can be used for environmental remediation through the photocatalytic degradation process. Modification of $ZnFe_2O_4$ with conjugated polymers such as polyaniline (PAni) with considerable carriers mobility and good optical properties can induce its photocatalytic activity.[35–37] Photosensitizer behavior of PAni under visible light illumination establishes the electron donor phenomenon in it, resulting in enhanced catalytic performance in PAni-contained hybrid heterostructures.[38,39] Developing plasmonic nanostructures based on $ZnFe_2O_4$ also can be used to increase the $ZnFe_2O_4$ catalyst activity. The surface plasmon resonance (SPR) effect observed in noble metals usually increases the light-harvesting ability of heterojunctions, resulting in considerable enhancement in the catalytic and photocatalytic activity.[40–42]

The objective of the current study is to develop a ternary plasmonic nanostructures system based on $ZnFe_2O_4$ through its combination with PAni and Ag NPs. The Ag@$ZnFe_2O_4$–PAni hybrid system was employed for the visible light photocatalytic application and recorded promising results. Results showed that the Ag@$ZnFe_2O_4$–PAni nanocomposites have efficient charge transfer, higher surface area, and higher light-harvesting ability due to synergistic effects of Ag NPs and PAni, resulting in higher photodegradation behavior than the $ZnFe_2O_4$ and $ZnFe_2O_4$–PAni materials. Moreover, the effect of the pH value of aqueous mediums, the initial concentration of dye, and the amount of photocatalyst were examined on the photocatalytic performance of the Ag@$ZnFe_2O_4$–PAni.

2 Experimental

2.1 Materials

All solvents and materials that used in this study were purchased from Merck and used as received without any more purification steps.

2.2 Synthesis of zinc ferrite material

To synthesize $ZnFe_2O_4$, 1.8 mmol of $Zn(CH_3COO)_2 \cdot 2H_2O$ and 2 mmol of $Fe(C_5H_7O_2)_3$ were dissolved in 10 mL of ethanol. In another vial, 10 mL of 2 mmol tetramethylammonium hydroxide pentahydrate (TMAH) solution in ethanol was prepared. Then, two solutions were added together and sonicated to obtain a dark red color solution. The obtained solution was exposed to microwave radiation at 180 °C for 45 min. The product was centrifuged and washed with ethanol. Finally, the brown precipitates were dried in a vacuum oven at 60 °C overnight, followed by calcination at 400 °C for 2 h to produce $ZnFe_2O_4$ NPs.

2.3 Synthesis of zinc ferrite–polyaniline material

To synthesize $ZnFe_2O_4$–PAni nanocomposite, an *in situ* polymerization technique was employed. 4 g of aniline material was dissolved into 200 mL of 1 M HCl solution by stirring for 2 h at a temperature of 50 °C. Then, 1.2 g $ZnFe_2O_4$ NPs were added to the aniline solution, followed by sonication for about 30 min at room temperature to homogenize the scattered $ZnFe_2O_4$ NPs. In another vial, 100 mL of 1 M HCl was carefully mixed with ammonium persulfate (APS) to obtain a 0.2 M solution. Then, the precooled APS solution was dropped wise to the aniline–$ZnFe_2O_4$ solution, followed by stirring at a temperature of 2 °C for 12 h to complete polymerization. The obtained solution was kept in the freezer overnight. Finally, the solution was filtered and washed with deionized water and methanol, followed by drying in a vacuum oven for 24 h at a temperature of 60 °C.

2.4 Synthesis of zinc ferrite–polyaniline decorated with silver nanoparticles

The Ag@$ZnFe_2O_4$–PAni plasmonic nanocomposites were synthesized through Ag^+ ions photoreduction in the $ZnFe_2O_4$–PAni aqueous solution (see Fig. 1). 400 mg of $ZnFe_2O_4$–PAni nanostructures were sonicated in 100 mL deionized water for 30 min to prepare a homogeneous suspension. Then, 40 mL of 2.5, 5, and 10 mM of $AgNO_3$ solution in deionized water were quickly added to $ZnFe_2O_4$–PAni aqueous solution in dark conditions. The suspensions were stirred for 2 h at room temperature in dark conditions and then exposed to natural sunlight for 90 min. The black precipitates were centrifuged and washed with deionized water and methanol repeatedly to remove impurities. The washed products were dried overnight in an oven at 60 °C for 24 h. The obtained powders were marked as AZP1, AZP2, and AZP3, referring to samples prepared using 2.5, 5, and 10 mM $AgNO_3$ solutions, respectively.

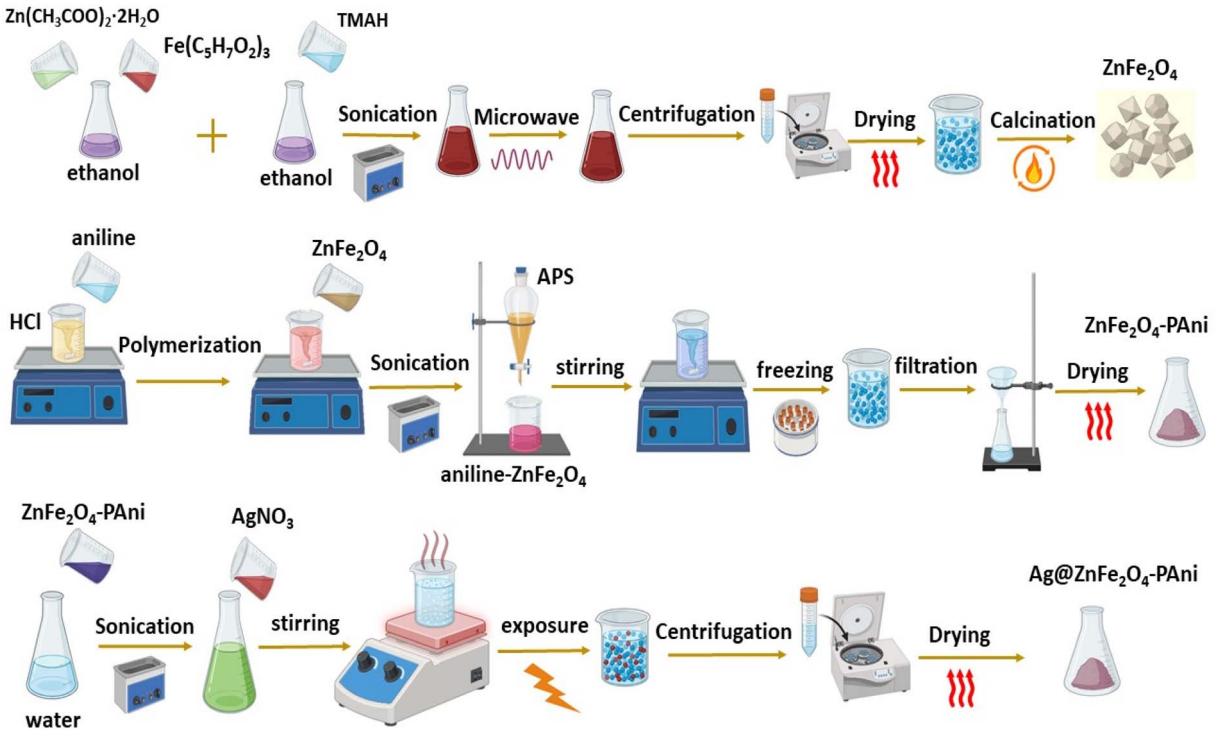

Fig. 1 Schematic diagram for preparation of Ag@$ZnFe_2O_4$–PAni nanocomposite.

2.5 Photocatalytic degradation investigation

The photocatalytic performance of the synthesized nanostructures for methylene blue (MB) or rhodamine B (RhB) dyes photodegradation was investigated by recording their UV-Vis spectra over reaction time under sunlight irradiance. For this test, 25 mg of MB or RhB dyes were dissolved into distilled water to obtain 25 ppm solutions. Then, 10 mg of photocatalyst materials ($ZnFe_2O_4$, $ZnFe_2O_4$–PAni, AZP1, AZP2, and AZP3) were dispersed into 100 mL dye solutions. The dye/photocatalyst material solutions were stirred under dark conditions for 30 min to establish an adsorption/desorption equilibrium between dye molecules and photocatalyst materials. Afterward, solutions were exposed to simulated sunlight illumination, and recorded their absorbance spectra. The same procedures were conducted to study the effects of pH and catalyst material concentration on the photodegradation performance of AZP2 material.

2.6 Characterizations

Crystalline structure of $ZnFe_2O_4$, $ZnFe_2O_4$–PAni, AZP1, AZP2, and AZP3 materials were measured by recording X-ray Diffraction (XRD) using a Rigaku Ultima IV XRD instrument. The morphology of the synthesized nanostructures were monitored using CM120 TEM and TESCAN Mira III FESEM. The FTIR spectra of materials were investigated using NICOLET-IS FTIR instrument. UV-vis spectra of samples were recorded using PerkinElmer Lambda Spectrometer. RAMAN spectra of materials were collected using a WiTec alpha 300 Raman spectrometer. The EIS response of samples were measured using Gamry Interface 1000 Potentiostat. PL spectra of material was collected using FLS 1000, Edinburgh spectrometer. Specific surface area of samples were measured by recording their Bet response using a BELSORP Mini II device. The transient photocurrent response of samples were measured using a PGSTAT302 N electrochemical workstation with a 500 W xenon lamp as the light source.

3 Results and discussion

Fig. 2 shows XRD patterns of different samples to confirm their successful synthesis. As shown in Fig. 2a, there are six peaks

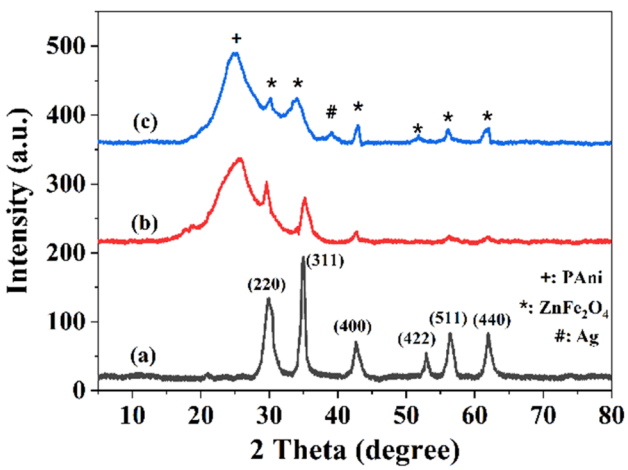

Fig. 2 XRD spectra of (a) $ZnFe_2O_4$, (b) $ZnFe_2O_4$–PAni, and (c) AZP2 nanostructures.

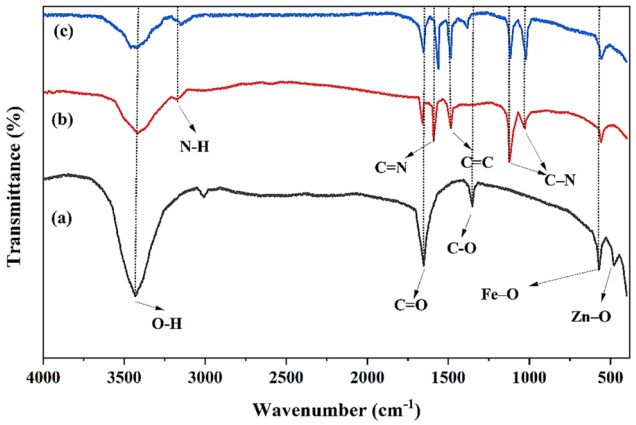

Fig. 3 FTIR spectra of (a) $ZnFe_2O_4$, (b) $ZnFe_2O_4$–PAni, and (c) AZP2 nanostructures.

positioned at 29.90°, 35°, 42.6°, 52.9°, 56.4°, and 62°, which are assigned to the (220), (311), (400), (422), (511), and (440) planes, respectively. These peaks align with the JCPDS file No. 00-022-1, confirming the formation of $ZnFe_2O_4$ NPs.[43] In the XRD pattern of $ZnFe_2O_4$–PAni (Fig. 2b), a broad peak at 25.7° is observed, attributing to the amorphous nature of PAni with the crystalline plane of (200). Besides, six peaks, referring to (220), (311), (400), (422), (511), and (440) planes of $ZnFe_2O_4$, are observed in the XRD pattern and prove the formation of $ZnFe_2O_4$–PAni hybrid structure. Fig. 2c shows XRD pattern of AZP2 material. In addition to the above-mentioned $ZnFe_2O_4$ and PAni phases, another peak is observed at 39.2° assigned to (111) Ag plane. It should be noted that the XRD peak of all the $ZnFe_2O_4$ NPs have minor shifts in AZP2, due to possible reaction of PAni and Ag with $ZnFe_2O_4$ material. These findings corroborate ternary Ag@$ZnFe_2O_4$–PAni plasmonic nanocomposites formation.

The FTIR spectra of $ZnFe_2O_4$, $ZnFe_2O_4$–PAni, AZP2 nanostructures are depicted in Fig. 3. The $ZnFe_2O_4$ spectrum encompasses five major peaks at 478.3 and 571.7 cm^{-1} attributed to vibrations of Fe–O and Zn–O bonds at octahedral and tetrahedral sites, 1351.5 cm^{-1} attributed to C–O stretching from residual synthesis precursors, and 1649.5 and 3430.9 cm^{-1} attributed to the bending and stretching vibrations of adsorbed water. In FTIR spectrum of $ZnFe_2O_4$–PAni (Fig. 2b), the characteristic peak of Fe–O in vanished, which can be caused by covering these bonds with the PAni molecules. In addition, five peaks at 1029.8 cm^{-1} assigned to secondary amine C–N stretching vibration, 1123.9 cm^{-1} assigned to vibration frequency of nitrogen quinone, 1484.2 cm^{-1} assigned to vibration for C=C bonds, 1593.1 cm^{-1} assigned to stretching mode of vibration for the C=N, and 3177.3 cm^{-1} assigned to the N–H stretching vibration. The AZP2 spectrum encompasses all peaks of $ZnFe_2O_4$–PAni with no more peaks. Notably, the nitrogen bonds shifted from 1129.7 cm^{-1} to 1021.8 cm^{-1} and N–H bonds shifted from 3177.3 cm^{-1} to 3146.7 cm^{-1}, indicating successful incorporation of Ag NPs to $ZnFe_2O_4$–PAni nanostructures.

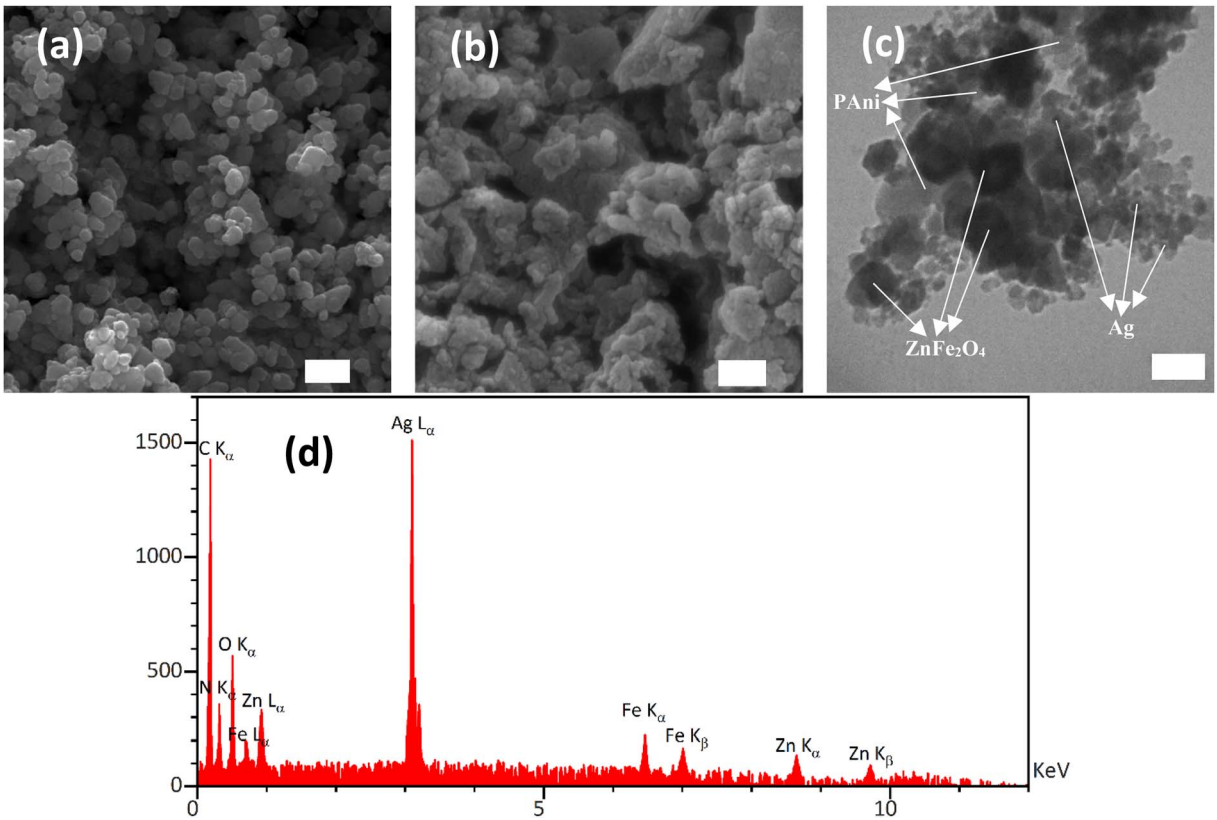

Fig. 4 FESEM image of (a) $ZnFe_2O_4$ and (b) AZP2. TEM image of (c) AZP2. (d) EDS elements mapping images of AZP2 composite. Scale bar of FESEM and TEM images are 200 nm and 80 nm, respectively.

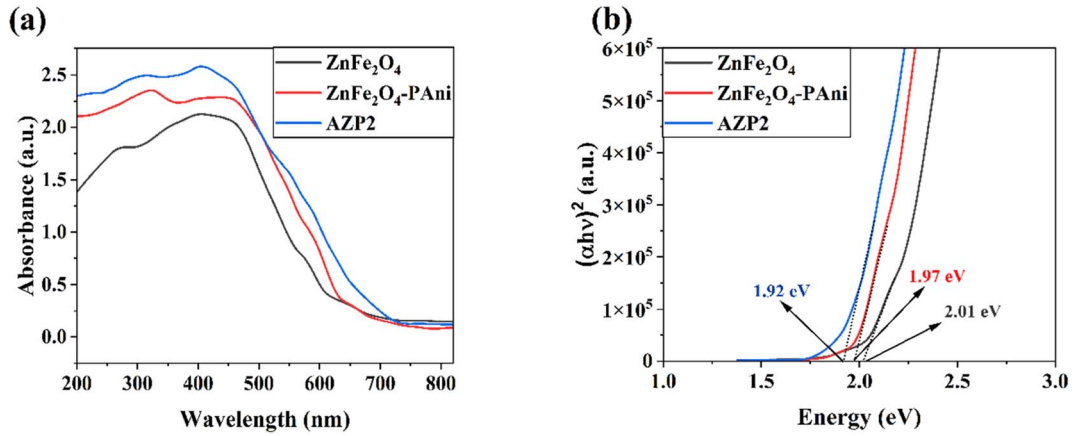

Fig. 5 (a) Absorbance spectra and (b) corresponding Tauc plots of $ZnFe_2O_4$, $ZnFe_2O_4$–PAni, and AZP2 nanostructures.

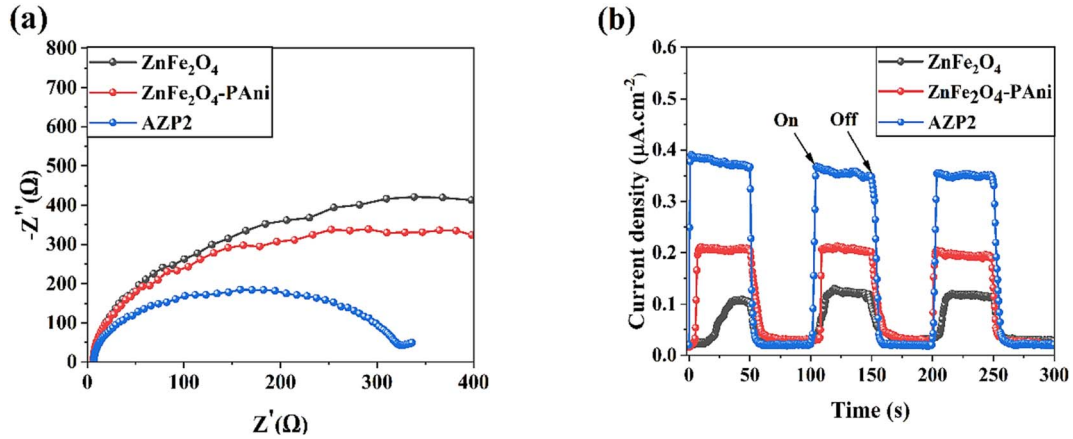

Fig. 6 (a) EIS spectra and (b) transient photocurrent response of $ZnFe_2O_4$, $ZnFe_2O_4$–PAni, and AZP2 nanostructures.

The FESEM images of samples were taken to investigate the surface morphology of $ZnFe_2O_4$ and AZP2 photocatalysts (Fig. 4a and b). The nano-sized $ZnFe_2O_4$ particles were aggregated due to the magnetic attraction forces among $ZnFe_2O_4$ (Fig. 4a). In Fig. 4b, it is evident that particles are highly agglomerated, which is possibly due to the incorporation of Ag NPs. The successful incorporation of Ag NPs into the $ZnFe_2O_4$–PAni nanostructures was evaluated by TEM (Fig. 3c). As can be seen, $ZnFe_2O_4$ NPs were capped with PAni molecules. Small Ag NPs attached on the $ZnFe_2O_4$ or PAni surfaces. Fig. 4d shows the EDS spectrum of the Ag@$ZnFe_2O_4$–PAni nanostructure. As seen, six elements of C, N, O, Fe, Zn, and Ag were observed in the sample, consistent with existing elements in the Ag@$ZnFe_2O_4$–PAni composite. It proves successful synthesis of the Ag@$ZnFe_2O_4$–PAni. Fig. 5a shows UV-Vis spectra of as-prepared photocatalyst materials. As can be seen, by incorporating Ag NPs into $ZnFe_2O_4$–PAni nanostructure, its light-harvesting behavior is increased. This phenomenon increases the potential of $ZnFe_2O_4$ to absorb exposed light and generate electron–hole charges. Fig. 5b depicts the corresponding Tauc plot of samples to investigate their optical bandgap energy. The optical bandgap for $ZnFe_2O_4$ is 2.01 eV, aligning with the reported value in literature.[44] Through the reaction of $ZnFe_2O_4$ with PAni materials, the optical bandgap is red-shifted to 1.97 eV and by the incorporation of Ag NPs to $ZnFe_2O_4$–PAni, it more reduced to 1.92 eV. It reveals that forming Ag@$ZnFe_2O_4$–PAni nanostructures can minimize the optical band gap of net $ZnFe_2O_4$ and increase light utilization, improving the photodegradation performance of $ZnFe_2O_4$ under visible light illumination.

Nyquist plots of samples using EIS method were obtained under light illumination to investigate the interfacial charge transfer resistance (Fig. 6a). By fitting the EIS spectra with the equivalent electrical circuit, parameters including series resistance (R_S) and charge transport resistance (R_{Ch}) were obtained. The EIS arc radius of AZP2 on the Nyquist plot is smaller than that of $ZnFe_2O_4$ and $ZnFe_2O_4$–PAni, which implies the AZP2 nanostructures have the lowest R_{Ch} value (87.8 Ω). It indicates a fast interfacial charge carrier transfer with high photogenerated carriers separation efficiency, which both are responsible for the enhanced photocatalytic activity of $ZnFe_2O_4$. It is due to the contribution of conjugated double bonds along the PAni structure and SPR effects of Ag NPs for the charge transfer mechanisms in AZP2 material. To get deeper insight on the photoelectrochemical properties of $ZnFe_2O_4$ NPs before and

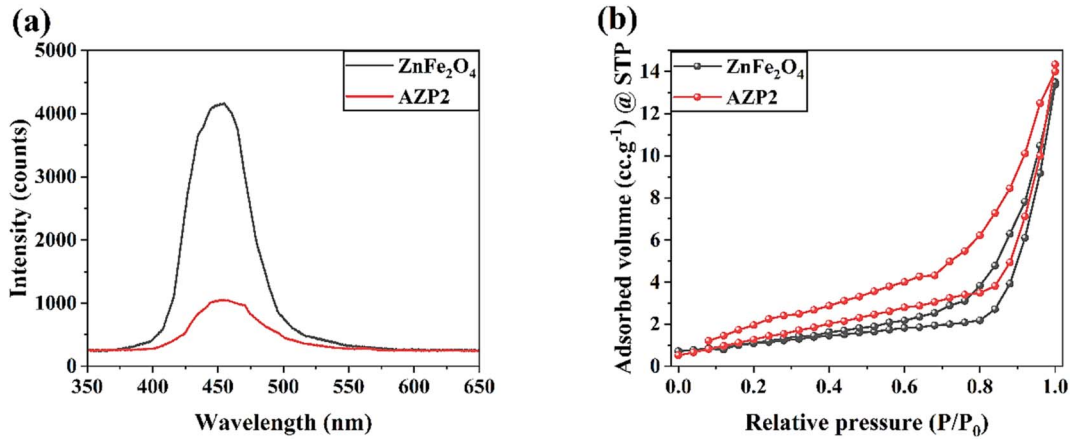

Fig. 7 (a) PL spectra and (b) BET curves of $ZnFe_2O_4$ and AZP2 nanostructures.

after modifications with PAni and Ag NPs, transient photocurrent response of $ZnFe_2O_4$ and $ZnFe_2O_4$–PAni, and AZP2 materials were investigated (Fig. 6b). As observed, the $ZnFe_2O_4$ sample implies a delayed photocurrent response upon the light is turned on and off. In contrast, the $ZnFe_2O_4$–PAni and AZP2 materials have rapid photocurrent responses. Moreover, results shows that the photocurrent of the $ZnFe_2O_4$–PAni electrode (0.213 mA cm^{-2}) is 67.7% higher than that of $ZnFe_2O_4$ (0.126 mA cm^{-2}), indicating the improved photoinduced electron–hole pairs separation efficiency in $ZnFe_2O_4$–PAni due to unique interfacial charge transfer of heterojunction. AZP2 shows the highest photocurrent density (0.358 mA cm^{-2}), indicating that the charge carrier separation in modified nanostructure of Ag@$ZnFe_2O_4$–PAni is further improved.

Fig. 7a shows PL spectra of $ZnFe_2O_4$ and AZP2 samples. The emission peak observed for both samples observed at 451 nm and indicates to the charge recombination.[45] As seen, the AZP2 has a weaken PL intensity than the pure $ZnFe_2O_4$, suggesting

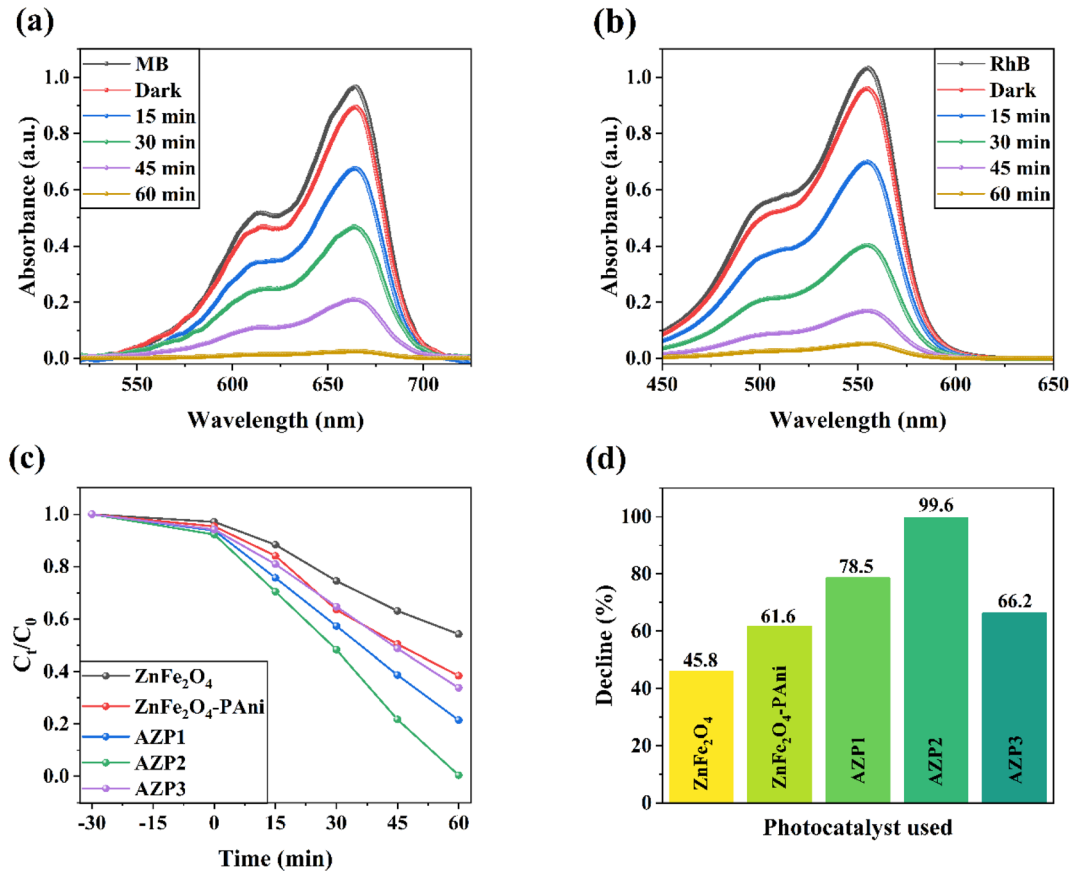

Fig. 8 Photocatalytic activity of AZP2 for (a) MB and (b) RhB dyes. (c) Kinetic plot *versus* illumination time for MB of $ZnFe_2O_4$, $ZnFe_2O_4$–PAni, AZP1, AZP2, and AZP3 nanostructures. (d) Comparison of MB degradation over different photocatalyst.

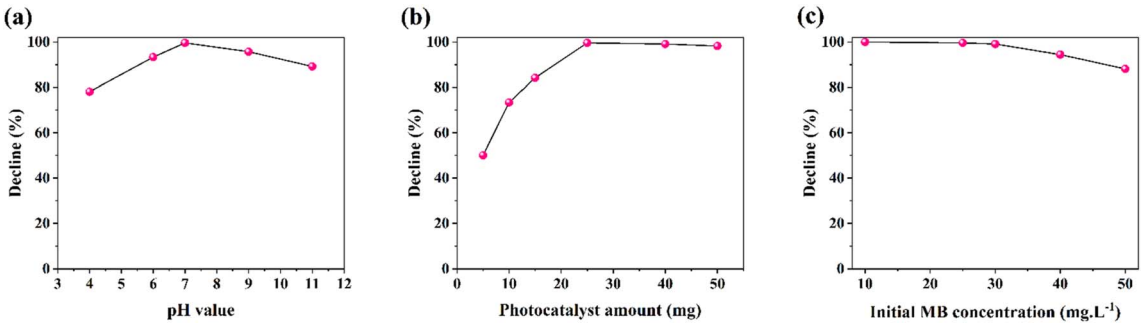

Fig. 9 (a) Effect of pH solution, (b) effect of photocatalyst amount and (c) effect of initial MB concentration on the photodegradation performance for AZP2.

reduced electron hole pair recombination rate in the AZP2 matrix.[46,47] It supports the EIS and transient photocurrent findings. The specific surface area of synthesized $ZnFe_2O_4$ and AZP2 nanostructures are measured using N_2 adsorption–desorption isotherm BET studies and depicted in Fig. 7b. The AZP2 material has a specific surface area of 12.34 $m^2 g^{-1}$, higher than the 7.41 $m^2 g^{-1}$ obtained for pure $ZnFe_2O_4$. Booted surface area is an important factor in increasing the photocatalytic activity of nanomaterials. In other words, the boosted surface area in nanomaterials increases the adsorption capacity for the pollutants on the material surface and active photocatalytic sites number, enhancing pollutant decomposition.[48,49] The photodegradation of MB and RhB dyes in aqueous medium was performed under simulated sunlight illumination for the AZP2 sample as the best photocatalyst was measured and depicted in Fig. 8a and b, respectively. The AZP2 plasmonic nanocomposites degraded 99.6% and 94.7% of MB and RhB molecules after exposure to light illumination for 60 min, respectively. Fig. 8c shows the degradation kinetics (C_t/C_0) for different photocatalysts to decompose MB dye during 60 min illumination. As shown, by increasing amounts of Ag NPs in Ag@$ZnFe_2O_4$–PAni structure, its photocatalyst activity is reduced; indicating optimum amounts of $AgNO_3$ solution during synthesis process is 5 mM. As represented in Fig. 8d, the photocatalytic activity of photocatalysts are follows the trend of AZP2 > AZP1 > AZP3 > $ZnFe_2O_4$–PAni > $ZnFe_2O_4$. It indicates that the employed method in here to advance photocatalytic performance of $ZnFe_2O_4$ has been very effective.

The solution pH value plays an important role in the photocatalytic-based reactions. The pH adjusting alters the interaction between the photocatalyst and dye molecules. Here, the photocatalytic activity of AZP2 nanostructures enhances from 78.1% to 99.6% as the pH value increases from 4 to 7 (Fig. 9a). By increasing the pH value to non-acidic conditions, the photocatalytic efficiency reduces to 89.2 (pH 11). Under acidic conditions (pH < 7), both Ag@$ZnFe_2O_4$–PAni and MB are positively charged, which results in a repulsive interaction in the solution and reduces photocatalytic activity. In neutral conditions, appropriate interactions between positively charged photocatalysts and MB enhance the photocatalytic activity. Under alkaline conditions, a slight reduction in the photocatalytic efficiency is observed, which is due to the interactions between anionic MB negatively charged photocatalysts. Next, effect of the initial AZP2 amount on the photocatalytic activity was investigated (Fig. 9b). For this aim, 5, 10, 15, 25, 40, and 50 mg of AZP2 nanostructures were dispersed in 100 mL of 25 ppm MB aqueous solution and their photocatalytic activities over 60 min light illumination were monitored. By enhancing the AZP2 amount, the MB photodegradation efficiency increased. The MB photodegradation efficiency started declining by raising the AZP2 amount to >40 mg, possibly due to the photocatalysts aggregation or more light scattering from photocatalyst nanoparticles.

Furthermore, effect of the initial MB concentration on the AZP2 photocatalytic performance was studied by varying MB concentration from 10 to 50 mg L^{-1} and probing their degradation efficiency. As shown in Fig. 9c, the photodegradation performance reduced from 100% (for 10 mg L^{-1}) to 88.1% (50 mg L^{-1}). The observed decline in performance is possibly due to the saturation of photocatalytic sites of AZP2 in high amounts of MB.

Reusability experiments were conducted for six successive runs (Fig. 10). After each photodegradation run, the AZP2-contained solution was centrifuged at 4000 rpm for 6 min. The collected AZP2 was washed with deionized water and methanol, followed by drying for 6 h at 75 °C. The dried AZP2

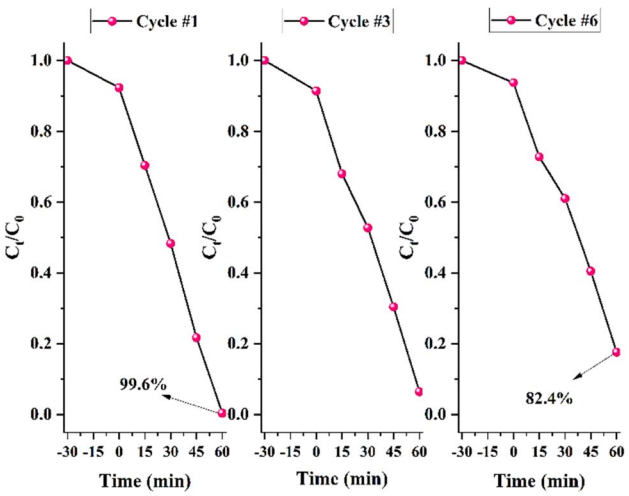

Fig. 10 Stability test of photodegradation of MB for AZP2.

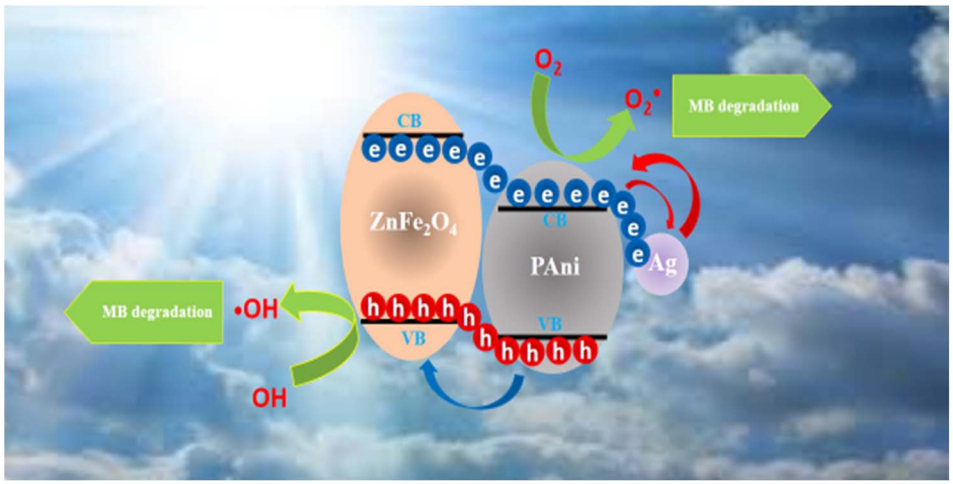

Fig. 11 Schematic view for possible photocatalytic mechanism behind Ag@$ZnFe_2O_4$–PAni nanocomposites for photo-degradation of dye molecules.

Table 1 Compare the obtained kinetic rate for MB degradation with literature

Photocatalyst	Kinetic rate (min^{-1})	Photocatalyst	Kinetic rate (min^{-1})
CeO_2/GO/PAM[50]	0.0259	ZnO[51]	0.0300
$MnTiO_3/TiO_2$ (ref. 52)	0.0059	$Bi_2O_3/MoSe_2$ (ref. 53)	0.0455
NiO/Ag/TiO_2 (ref. 54)	0.0312	rGO/WO_3 (ref. 55)	0.0073
Ag_2O[56]	0.0319	g-$C_3N_4/CoFe_2O_4$ (ref. 57)	0.0190
CdSe[58]	0.0380	This study	0.0406

was again used for reusability test. As can be seen, a photocatalytic performance of 99.6% and 96.6% was recorded for the first and second cycles; however, in total a ~17% decline in photocatalytic performance was observed after six runs. The reusability test implies that the Ag@$ZnFe_2O_4$–PAni plasmonic nanocomposites can be used for photodegradation of industrial aqueous wastes.

The possible photodegradation mechanism of the Ag@$ZnFe_2O_4$–PAni system is depicted in Fig. 11. By exposing sunlight illumination to the Ag@$ZnFe_2O_4$–PAni/dye aqueous solution, the $ZnFe_2O_4$ valence band (VB) electrons absorb light energy and generate hot electrons. Next, these hot electrons inject into the conduction band of PAni polymer, then moved to Ag NPs surface. Theses hot electrons react with surrounding O_2 and form superoxide radicals ($O_2^{\bullet}$). The $O_2^{\bullet}$ radicals assist to form the hydroxyl radicals ($^{\bullet}OH$). In addition, the holes from the PAni molecules transfer to the VB of $ZnFe_2O_4$, which contribute to the $^{\bullet}OH$ radicals formation. Then, the $^{\bullet}OH$ and $O_2^{\bullet}$ radicals decompose the dye molecules.

Table 1 summarizes the kinetic rate values provided for several types of nanocomposites and compares them with the values acquired in this work.

4 Conclusions

In the current study, $ZnFe_2O_4$ photocatalytic activity was increased by developing Ag@$ZnFe_2O_4$–PAni plasmonic nanostructures. The synthesized Ag@$ZnFe_2O_4$–PAni nanostructures was employed to photodegradation of MB and RhB dyes under simulated sunlight illumination. Results showed the ternary nanostructures exhibit higher photocatalytic efficiency than that of the pure $ZnFe_2O_4$ ferrites. After 60 min light illumination, Ag@$ZnFe_2O_4$–PAni plasmonic nanostructures decomposed 99.6% of MB dye. Incorporating Ag NPs into to $ZnFe_2O_4$–PAni nanocomposites boosted light-harvesting photocatalyst and reduced energy bandgap from 2.01 eV to 1.92 eV. These phenomenons increased the electron–hole production rate in $ZnFe_2O_4$ by exposure it to light. Moreover, contribution Ag NPs and PAni to charge transfer mechanisms boosted charge separation during photocatalytic process. The Ag@$ZnFe_2O_4$–PAni plasmonic nanostructures offered larger surface area and photocatalytic sites than the pure $ZnFe_2O_4$. Overall, enlarged surface area, increased electron–hole production rate, and boosted charge separation are the origins of photocatalytic improvement of $ZnFe_2O_4$. Furthermore, the Ag@$ZnFe_2O_4$–PAni photocatalyst with its considerable reusability can be used in industries to photodegrade their aqueous wastes. In addition, the obtained results show that by modification $ZnFe_2O_4$ materials with metallic dopants and by developing $ZnFe_2O_4$–polymer hybrid systems can design efficient photocatalyst materials to waste water treatments.

Data availability

The datasets used and/or analysed during the current study available from the corresponding author on reasonable request.

Author contributions

Conceptualization, methodology, formal analysis, investigation, data curation, validation; visualization, original draft preparation, writing–review and editing M. K. A. M., A. M. N., S. S. J., R. I. F., O. A. N. All authors reviewed the manuscript.

Conflicts of interest

The authors declare no conflict of interest.

References

1 H. M. Al-Attar, H. T. Hussein, R. S. Zamel, A. J. Addie and M. K. Mohammed, Methylene blue degradation using ZnO: CuO: Al2O3 nanocomposite synthesized by liquid laser ablation, *Opt. Quantum Electron.*, 2023, **55**, 309.

2 R. I. Faeq, S. S. Jaafar, A. M. Naji, M. K. Mohammed and O. A. Nief, Increasing the photocatalytic degradation rate of a rGO/PVA nanocomposite decorated with ZnO nanoparticles, *New J. Chem.*, 2023, **47**, 13661–13670.

3 A. M. Naji, I. Y. Mohammed, S. H. Mohammed, M. K. Mohammed, D. S. Ahmed, M. S. Jabir and A. M. Rheima, Photocatalytic degradation of methylene blue dye using F doped ZnO/polyvinyl alcohol nanocomposites, *Mater. Lett.*, 2022, **322**, 132473.

4 R. I. Faeq, S. S. Jaafar, A. M. Naji, M. K. Mohammed and O. A. Nief, Investigation of the visible-light-driven catalytic activity of nickel oxide-doped carbon nanotubes/polyvinylpyrrolidone nanocomposites towards methylene blue dye, *Inorg. Chem. Commun.*, 2023, **157**, 111390.

5 J. Karpińska and U. Kotowska, *Removal of Organic Pollution in the Water Environment*, MDPI, 2019, p. 2017.

6 D. Han and M. J. Currell, Persistent organic pollutants in China's surface water systems, *Sci. Total Environ.*, 2017, **580**, 602–625.

7 A. G. Heath, *Water Pollution and Fish Physiology*, CRC press, 2018.

8 E. Molahosseini, M. Molaei, H. Zare and F. Farahmandzadeh, A novel dark catalyst material based on Fe3O4/MWCNT/SiO2 magnetic nanocomposite for simple and ultrafast degradation of methylene blue, *Mater. Res. Bull.*, 2024, **170**, 112571.

9 A. Ahmadpour, Using of activated carbon adsorption in wastewater industries, *J. Chem. Lett.*, 2022, **3**, 2–9.

10 J. Kim, S. Yoon, M. Choi, K. J. Min, K. Y. Park, K. Chon and S. Bae, Metal ion recovery from electrodialysis-concentrated plating wastewater via pilot-scale sequential electrowinning/chemical precipitation, *J. Cleaner Prod.*, 2022, **330**, 129879.

11 A. George, A. D. Raj, A. A. Irudayaraj, R. Josephine, X. Venci, S. J. Sundaram, R. Rajakrishnan, P. Kuppusamy and K. Kaviyarasu, Regeneration study of MB in recycling runs over nickel vanadium oxide by solvent extraction for photocatalytic performance for wastewater treatments, *Environ. Res.*, 2022, **211**, 112970.

12 K. Hussain, N. A. Khan, V. Vambol, S. Vambol, S. Yeremenko and V. Sydorenko, Advancement in Ozone base wastewater treatment technologies: Brief review, *Ecol. Quest.*, 2022, **33**, 7–19.

13 S. Lahiri, C. Zhang, M. Sillanpää and L. Liu, Nanoporous NiO@ SiO2 photo-catalyst prepared by ion-exchange method for fast elimination of reactive dyes from wastewater, *Mater. Today Chem.*, 2022, **23**, 100677.

14 Y. Wu, X. He, X. Wang, J. Xv, M. Muddassir, I. A. Ansari and A. Zhong, Synergistic efficacy unleashed: Co/Ni-based catalysts as a versatile powerhouse for photocatalytic degradation of ornidazole, *Inorg. Chim. Acta*, 2024, **568**, 122115.

15 I. Ahmad, M. A. Aftab, A. Fatima, S. D. Mekkey, S. Melhi and S. Ikram, A comprehensive review on the advancement of transition metals incorporated on functional magnetic nanocomposites for the catalytic reduction and photocatalytic degradation of organic pollutants, *Coord. Chem. Rev.*, 2024, **514**, 215904.

16 W. Guo, T. Guo, Y. Zhang, L. Yin and Y. Dai, Progress on simultaneous photocatalytic degradation of pollutants and production of clean energy: A review, *Chemosphere*, 2023, 139486.

17 X. Lu, K. Xu, P. Chen, K. Jia, S. Liu and C. Wu, Facile one step method realizing scalable production of gC 3 N 4 nanosheets and study of their photocatalytic H 2 evolution activity, *J. Mater. Chem. A*, 2014, **2**, 18924–18928.

18 E. Y. Salih, Z. Abbas, S. H. H. Al Ali and M. Z. Hussein, Dielectric Behaviour of Zn/Al-NO3 LDHs Filled with Polyvinyl Chloride Composite at Low Microwave Frequencies, *Adv. Mater. Sci. Eng.*, 2014, **2014**, 647120.

19 M. Dehghanipour, M. Khanzadeh, M. Karimipour and M. Molaei, Dependence of nonlinear optical properties of Ag2S@ ZnS core-shells on Zinc precursor and capping agent, *Opt Laser. Technol.*, 2018, **100**, 286–293.

20 S. Perumal, M. K. Mohammed, M. Govindasamy, A. A. Alothman, M. Ouladsmane and R. Ganesan, An ultra-high electrochemical performance of surface-rich boron induced multi-metal centered heterocatalyst for overall water splitting, *Int. J. Hydrogen Energy*, 2024, **54**, 652–664.

21 S. O. Abdulghani, E. Y. Salih and A. S. Mohammed, Fabrication and photo-responsive characteristics of GeO2 doped SnO2/porous Si film for ultraviolet photodetector application, *Mater. Chem. Phys.*, 2023, **303**, 127859.

22 O. Aldaghri, E. Y. Salih, A. Ramizy, A. S. Mohammed, K. H. Ibnaouf and M. H. Eisa, Rapid fabrication of fast response CdS/Si visible light photodetector: Influence of laser energy, *Res. Phys.*, 2023, **54**, 107112.

23 M. B. A. Bashir, S. M. Said, M. F. M. Sabri, Y. Miyazaki, D. A. Shnawah, M. Shimada, M. F. M. Salleh, M. S. Mahmood, E. Y. Salih and F. Fitriani, In-filled La 0.5 Co 4 Sb 12 skutterudite system with high thermoelectric figure of merit, *J. Electron. Mater.*, 2018, **47**, 2429–2438.

24 X. Qiu, Y. Zhang, Y. Zhu, C. Long, L. Su, S. Liu and Z. Tang, Applications of nanomaterials in asymmetric photocatalysis: recent progress, challenges, and opportunities, *Adv. Mater.*, 2021, **33**, 2001731.

25 A. Arimi, L. Megatif, L. I. Granone, R. Dillert and D. W. Bahnemann, Visible-light photocatalytic activity of zinc ferrites, *J. Photochem. Photobiol., A*, 2018, **366**, 118–126.
26 O. K. Mmelesi, N. Masunga, A. Kuvarega, T. T. Nkambule, B. B. Mamba and K. K. Kefeni, Cobalt ferrite nanoparticles and nanocomposites: Photocatalytic, antimicrobial activity and toxicity in water treatment, *Mater. Sci. Semicond. Process.*, 2021, **123**, 105523.
27 Q. Zhang, Z. Li, X. Li, L. Yu, Z. Zhang and Z. Wu, Preparation of cobalt ferrite nanoparticle-decorated boron nitride nanosheet flame retardant and its flame retardancy in epoxy resin, *Nano*, 2019, **14**, 1950063.
28 P. Thakur, S. Taneja, D. Chahar, B. Ravelo and A. Thakur, Recent advances on synthesis, characterization and high frequency applications of Ni-Zn ferrite nanoparticles, *J. Magn. Magn. Mater.*, 2021, **530**, 167925.
29 N. Yadav, L. Chaudhary, P. Sakhare, T. Dongale, P. Patil and A. Sheikh, Impact of collected sunlight on ZnFe2O4 nanoparticles for photocatalytic application, *J. Colloid Interface Sci.*, 2018, **527**, 289–297.
30 G. Fan, J. Tong and F. Li, Visible-light-induced photocatalyst based on cobalt-doped zinc ferrite nanocrystals, *Ind. Eng. Chem. Res.*, 2012, **51**, 13639–13647.
31 R. Yu, J. Zhao, Z. Zhao and F. Cui, Copper substituted zinc ferrite with abundant oxygen vacancies for enhanced ciprofloxacin degradation via peroxymonosulfate activation, *J. Hazard. Mater.*, 2020, **390**, 121998.
32 B. Janani, A. Syed, L. Sruthi, P. Sivaranjani, A. M. Elgorban, A. H. Bahkali, N. S. Zaghloul, M. M. Badawy, A. Das and S. S. Khan, Visible light driven photocatalytic activity and efficient antibacterial activity of ZnFe2O4 decorated CdO nanohybrid heterostructures synthesized by ultrasonic-assisted method, *Colloids Surf., A*, 2021, **628**, 127307.
33 C. Akshhayya, M. K. Okla, A. M. Thomas, A. A. AL-ghamdi, M. A. Abdel-Maksoud, B. Almunqedhi, H. AbdElgawad, L. L. Raju and S. S. Khan, Insights into photocatalytic mechanism for the rational design of pn heterojunction by decorating mesoporous SnS2 over ZnFe2O4 nanocomposite for accelerated visible light photocatalysis, *Mater. Chem. Phys.*, 2022, **277**, 125464.
34 N. Kaushal, S. Sarraf, A. K. Basu, S. Mishra and A. Saha, Facile microwave synthesis of Zinc Ferrite@ NCDs for photocatalytic degradation of fluoroquinolone antibiotics, *Mater. Chem. Phys.*, 2024, **314**, 128823.
35 H. Mohseni, M. Dehghanipour, N. Dehghan, F. Tamaddon, M. Ahmadi, M. Sabet and A. Behjat, Enhancement of the photovoltaic performance and the stability of perovskite solar cells via the modification of electron transport layers with reduced graphene oxide/polyaniline composite, *Sol. Energy*, 2021, **213**, 59–66.
36 A. M. Naji, S. H. Kareem, A. H. Faris and M. K. Mohammed, Polyaniline polymer-modified ZnO electron transport material for high-performance planar perovskite solar cells, *Ceram. Int.*, 2021, **47**, 33390–33397.
37 Z. T. M. Noori, A. M. Naji, O. A. Nief, M. K. Mohammed, N. M. Ahmed and S. Singh, Polyaniline/Nickle oxide hole transport layers to increase stability and efficiency of regular perovskite solar cells, *Int. J. Energy Res.*, 2022, **46**, 17285–17294.
38 Q. Wang, J. Hui, J. Li, Y. Cai, S. Yin, F. Wang and B. Su, Photodegradation of methyl orange with PANI-modified BiOCl photocatalyst under visible light irradiation, *Appl. Surf. Sci.*, 2013, **283**, 577–583.
39 Q. Mo, S. Zeng, J. Yang, C. Wu and Y. Zhang, Polyaniline-ferrite nanocomposite as a new magnetically recyclable photocatalyst with enhanced photocatalytic activity, *J. Ceram. Soc. Jpn.*, 2020, **128**, 135–141.
40 S. Choudhary and S. Mohapatra, Boosting sunlight driven photocatalytic and catalytic performance of $ZnFe_2O_4$-ZnO nanohybrids by loading Ag nanoparticles, *J. Photochem. Photobiol., A*, 2024, 115797.
41 C. Karunakaran, I. JebaSing and P. Vinayagamoorthy, Synthesis of superparamagnetic ZnFe2O4-core/Ag-deposited ZnO-shell nanodiscs for application as visible light photocatalyst, *J. Nanosci. Nanotechnol.*, 2019, **19**, 4064–4071.
42 S. Choudhary, A. Bisht, B. Satpati and S. Mohapatra, Facile synthesis of Ce-doped ZnO nanospindles for photocatalytic applications, *Appl. Phys. A: Mater. Sci. Process.*, 2021, **127**, 1–14.
43 P. Dolcet, K. Kirchberg, A. Antonello, C. Suchomski, R. Marschall, S. Diodati, R. Muñoz-Espí, K. Landfester and S. Gross, Exploring wet chemistry approaches to ZnFe 2 O 4 spinel ferrite nanoparticles with different inversion degrees: a comparative study, *Inorg. Chem. Front.*, 2019, **6**, 1527–1534.
44 S. Sasikumar and A. Rajaram, The synergetic effect of cobalt-doped zinc ferrite and hexagonal boron nitride photocatalyst for wastewater treatment, *Diamond Relat. Mater.*, 2024, 111270.
45 M. Shakil, U. Inayat, M. Ashraf, M. Tanveer, S. Gillani and A. Dahshan, Photocatalytic performance of novel zinc ferrite/copper sulfide composites for the degradation of Rhodamine B dye from wastewater using visible spectrum, *Optik*, 2023, **272**, 170353.
46 N. Khadgi, A. R. Upreti and Y. Li, Simultaneous bacterial inactivation and degradation of an emerging pollutant under visible light by ZnFe 2 O 4 co-modified with Ag and rGO, *RSC Adv.*, 2017, **7**, 27007–27016.
47 A. Kar, P. Dagar, S. Kumar, I. S. Deo, G. V. Prakash and A. K. Ganguli, Photoluminescence and lifetime studies of C-dot decorated CdS/ZnFe2O4 composite designed for photoelectrochemical applications, *J. Photochem. Photobiol., A*, 2023, **439**, 114612.
48 A. Singh, F. Wan, K. Yadav, S. Kharbanda, P. Thakur and A. Thakur, A novel magnetic NiFe2O4-Ag-ZnO hybrid nanocomposite for the escalated photocatalytic dye degradation and antibacterial activities, *Mater. Sci. Eng., B*, 2024, **299**, 116935.
49 M. M. J. Sadiq, U. S. Shenoy and D. K. Bhat, NiWO4-ZnO-NRGO ternary nanocomposite as an efficient photocatalyst for degradation of methylene blue and reduction of 4-nitro phenol, *J. Phys. Chem. Solids*, 2017, **109**, 124–133.

50 Z. Kalaycıoğlu, B. Özuğur Uysal, O. N. Pekcan and F. B. Erim, Efficient photocatalytic degradation of methylene blue dye from aqueous solution with cerium oxide nanoparticles and graphene oxide-doped polyacrylamide, *ACS Omega*, 2023, **8**, 13004–13015.

51 R. H. Waghchaure, V. A. Adole and B. S. Jagdale, Photocatalytic degradation of methylene blue, rhodamine B, methyl orange and Eriochrome black T dyes by modified ZnO nanocatalysts: A concise review, *Inorg. Chem. Commun.*, 2022, **143**, 109764.

52 S. Alkaykh, A. Mbarek and E. E. Ali-Shattle, Photocatalytic degradation of methylene blue dye in aqueous solution by MnTiO3 nanoparticles under sunlight irradiation, *Heliyon*, 2020, **6**(4), e03663.

53 M. Alahmadi, W. H. Alsaedi, W. Mohamed, H. M. Hassan, M. Ezzeldien and A. M. Abu-Dief, Development of Bi2O3/MoSe2 mixed nanostructures for photocatalytic degradation of methylene blue dye, *J. Taibah Univ. Sci.*, 2023, **17**, 2161333.

54 W. Mohammed, M. Matalkeh, R. M. Al Soubaihi, A. Elzatahry and K. M. Saoud, Visible light photocatalytic degradation of methylene blue dye and pharmaceutical wastes over ternary NiO/Ag/TiO2 heterojunction, *ACS Omega*, 2023, **8**, 40063–40077.

55 V. Ramar and K. Balasubramanian, Reduced graphene oxide/WO3 nanorod composites for photocatalytic degradation of methylene blue under sunlight irradiation, *ACS Appl. Nano Mater.*, 2021, **4**, 5512–5521.

56 S. Sagadevan, S. F. Alshahateet, J. A. Lett, I. Fatimah, R. P. Sivasankaran, A. K. Sibhatu, E. Leonard, M.-V. Le and T. Soga, Highly efficient photocatalytic degradation of methylene blue dye over Ag2O nanoparticles under solar light irradiation, *Inorg. Chem. Commun.*, 2023, **148**, 110288.

57 H. D. Weldekirstos, T. Mengist, N. Belachew and M. L. Mekonnen, Enhanced photocatalytic degradation of methylene blue dye using fascily synthesized g-C3N4/CoFe2O4 composite under sun light irradiation, *Res. Chem.*, 2024, **7**, 101306.

58 P. Gharbani, A. Mehrizad and S. A. Mosavi, Optimization, kinetics and thermodynamics studies for photocatalytic degradation of Methylene Blue using cadmium selenide nanoparticles, *npj Clean Water*, 2022, **5**, 34.